A. Zarketa-Astigarraga, R. Manzanares-Bercial, A. Martínez-Cava, A. Martin-Mayor, M. Martinez-Agirre, M. Penalba; On the mitigation of detrimental effects via passive flow-control devices in aerodynamic airfoils operating under turbulence and surface degradation effects. Physics of Fluids 1 April 2026; 38 (4): 044112.

https://doi.org/10.1063/1.5007974

On the mitigation of detrimental effects via passive flow-control devices in aerodynamic airfoils operating under turbulence and surface degradation effects

A. Zarketa-Astigarraga,[1] R. Manzanares-Bercial,[2] A. Martínez-Cava,[2] A. Martin-Mayor,[1] M. Martinez-Agirre,[1] and M. Penalba[1, a)]

[1)] *Mondragon Unibertsitatea, Faculty of Engineering, Mechanical and Industrial Production, Loramendi 4, Mondragon 20500 Gipuzkoa, Spain*

[2)] *Instituto Universitario "Ignacio Da Riva" (IDR/UPM), Universidad Politécnica de Madrid, Plaza Cardenal Cisneros, 3, E.28040, Madrid, Spain*

(*Electronic mail: azarketa@mondragon.edu)

(Dated: 18 March 2026)

This work investigates how moderate turbulence and surface roughness jointly affect the aerodynamics of a NACA0021 airfoil operating at transitional Reynolds numbers ($\mathrm{Re} = 0.8$–1.2×10^5). Wind-tunnel tests were performed under two controlled flow paradigms: a low-disturbance *Clean* condition and a *Combined* condition including both freestream turbulence ($I \approx 3.8\%$) and leading-edge roughness. In addition to the baseline (*Bare*) configuration, two unilateral passive-device layouts were tested, with triangular protrusions placed at $x/c = 0.25$ (*PD25*) and $x/c = 0.5$ (*PD50*).

Results show that the *Combined* inflow linearises the lift curve and softens stall but reduces lift slope and aerodynamic efficiency by up to 60% compared with the *Clean* baseline. The effect of the passive devices depends on their position and on Re: *PD25* can delay stall and recover efficiency at high angles of attack, while *PD50* offers only limited or negative impact once the boundary layer becomes fully turbulent. Overall, the findings demonstrate that turbulence–roughness interactions dominate aerodynamic behaviour at transitional scales, and that small passive elements can provide only local improvements. These results underline the need to assess low-Re airfoils under realistic inflow conditions when developing flow-control strategies for distributed or urban wind-energy systems.

I. INTRODUCTION

A. Context and motivation

The global transition toward renewable energy continues to accelerate, and wind power remains one of the primary pillars of decarbonization strategies. According to the *Global Wind Report 2025* issued by the Global Wind Energy Council (GWEC), a record 117 GW of new capacity was installed in 2024, bringing the worldwide cumulative capacity to approximately 1.13 TW[1]. These figures confirm a steady and geographically diversified expansion driven by both offshore and onshore markets[1,2].

While the upscaling of large offshore machines has pushed rotor diameters beyond 250 m and rated powers above 20 MW[3,4], a complementary trend has emerged at smaller scales. Mid- and small-scale systems are increasingly integrated into hybrid or urban installations[5,6], where they encounter flow environments markedly different from those of utility-scale farms. Because of their smaller characteristic dimensions, the associated airfoils operate within a Reynolds-number range typically between 5×10^4 and 5×10^5, where laminar, transitional, and turbulent regimes coexist. Within this interval, aerodynamic performance becomes highly sensitive to both external disturbances and surface condition[7,8]. Even minor variations in turbulence intensity or local roughness can shift stall onset or modify lift and drag behaviour significantly.

A deeper understanding of these dependencies is crucial not only for improving efficiency and control, but also for providing physical validation to computational models that attempt to capture transitional dynamics[9,10]. This context motivates the present experimental work, which isolates and analyses the combined aerodynamic effects of freestream turbulence and surface roughness under controlled laboratory conditions.

B. Aerodynamic behaviour under turbulence and surface roughness

At transitional Reynolds numbers, both the boundary-layer evolution and the laminar–turbulent transition can depend sensitively on a set of parameters that may be ascribed either to external disturbances or to the surface condition of the airfoil. In addition to turbulence intensity and surface roughness, relevant aerodynamic factors include the local pressure-gradient history, surface curvature, the turbulence integral length scale and unsteady inflow effects such as angle-of-attack fluctuations and wake perturbations. The present work focuses specifically on isolating the effects of turbulence intensity and surface roughness under controlled wind-tunnel conditions[7,8,11–14], while the baseline geometry of the airfoil (which synthesizes the local pressure-gradient and the surface curvature effects) is fixed throughout the experimental campaign. Potential dynamic effects such as angle-of-attack fluctuations or wake perturbations are not considered in the study.

As such, the transitional behaviour of the airfoil is strongly influenced by the characteristics of the incoming disturbances and by the surface condition. In a set of previous studies, the

[a)] Also at Ikerbasque, Basque Foundation for Science, Euskadi Plaza 5, 48011 Bilbao, Spain

authors have shown that laminar-separation bubbles (LSBs) form on a NACA0021 geometry at transitional Reynolds numbers in the $[0.8, 1.2] \cdot 10^5$ range, and that the bubble progressively migrates towards the leading edge as the angle of attack increases, until it bursts in the vicinity of stall[15]. They further reported that the relatively large thickness of the NACA0021 section promotes a coupled evolution in which the forward motion of the LSB is accompanied by a gradual trailing-edge flow detachment, with the onset of stall being governed by the interplay between these two mechanisms[15,16]. Importantly, those studies also showed that both elevated free-stream turbulence and surface roughness can markedly alter this transition scenario: by promoting earlier transition, they can suppress the formation of the LSB and shift the stalling behavior towards a predominantly trailing-edge-detachment mechanism[16,17].

Freestream turbulence effects on the aerodynamic behavior of transitionally-operating airfoils are amply reported in the literature. Small-scale flight systems such as MAVs and UAVs operate in the highly turbulent atmospheric boundary layer (ABL), where large eddies impose continuous fluctuations on local incidence. Watkins et al.[18,19] and later[20] showed that when the turbulence integral scale is of the same order as the chord, unsteady forcing accelerates transition and modifies separation dynamics. Similar mechanisms affect small near-surface aerodynamic devices, in which turbulence intensities can reach 20–30 % depending on terrain and obstacles[21–23]. These fluctuations induce dynamic-stall behaviour and fatigue-related unsteadiness.

The aerodynamic implications of surface roughness have been extensively studied in turbomachinery, where even limited erosion or deposition can severely alter blade performance. Bons[24] reviewed seven decades of work and demonstrated that roughness enhances heat transfer yet precipitates earlier transition and higher drag. Subsequent research has refined roughness-characterization metrics and measurement standards[25,26], though challenges remain in linking surface parameters to aerodynamic response at transitional scales. Recent studies[9,10] highlight that the roughness spectrum, rather than the mean height alone, can govern instability amplification and intermittency. When it comes to the wind-turbine sector, surface degradation caused by rain, insects, dust, or erosion further compounds these effects. Numerous studies[6,27–35] have shown that roughness concentrated near the leading edge can halve the lift-to-drag ratio even at low tip speed ratios. The roughness–turbulence interaction is non-linear: turbulence can either mask or amplify roughness effects depending on scale ratios, while roughness alters the receptivity of the boundary layer to external fluctuations. Despite its evident importance, this coupling has received limited systematic investigation. Controlled experiments that reproduce both effects concurrently—–using passive grids for turbulence generation[36,37] and calibrated roughness treatments—are therefore essential for realistic aerodynamic characterization.

Likewise, the problem being addressed herein holds immediate practical importance for the wind-turbine industry, particularly at small and mid scales where transitional aerodynamics dominate. Devices operating in urban, hybrid, or near-surface environments experience turbulence levels far above those seen in utility-scale farms[21–23], while also being exposed to rapid surface degradation from insects, dust, rain erosion or particulate deposition[27–30]. Such conditions can precipitate early transition, modify laminar-separation-bubble dynamics, and shift stall onset markedly[7,11–14]. Because these effects are strongly nonlinear, turbulence may either mask or amplify roughness-induced penalties[9,10], complicating the prediction of aerodynamic performance using standard low-Reynolds-number models. These industrial challenges have motivated growing interest in passive flow-control concepts—such as textured or patterned surfaces and discrete-roughness elements[29,38–40]—whose robustness must be assessed under realistic disturbances rather than idealized inflows. Accordingly, laboratory studies capable of jointly controlling turbulence intensity, roughness characteristics, and measurement precision are essential to support the development of reliable low-order aerodynamic models, inform design choices for small-scale rotors, and ultimately enhance the performance and durability of wind-energy systems operating in highly perturbed environments.

C. Flow-control strategies for transitional regimes

Transitional flows, being highly receptive to disturbances, are also particularly responsive to flow-control strategies. Such strategies aim to stabilise or tailor the boundary layer to delay separation and improve aerodynamic efficiency. They are broadly classified as *active* or *passive*.

Active methods, including plasma actuators[14,41,42], micro-electro-mechanical devices[43,44], and acoustic excitation[45,46], can adapt to changing conditions but require external power and complex integration. Passive approaches are simpler and energetically self-sustained, relying instead on geometric or surface modifications. Examples include riblet or textured coatings[29,38,47,48], and discrete-roughness elements such as vortex generators or surface protrusions[39,40,49–52]. Although their operating principles differ, most act by energising the near-wall flow, altering shear-layer growth, or redistributing pressure gradients.

Previous assessments of these devices have generally been conducted under idealized, low-disturbance inflows. As a result, their robustness under more realistic conditions—where turbulence and surface roughness coexist—remains uncertain. Addressing this gap requires experimental configurations that combine controlled turbulence, prescribed surface roughness, and precise force and wake measurements.

The present study continues the authors' previous investigations[8,16] and focuses exclusively on airfoil-level aerodynamics within the transitional regime. A passive discrete-roughness concept is applied to a NACA 0021 profile and tested across several Reynolds numbers and flow paradigms, ranging from a *Clean* baseline to a *Combined* configuration incorporating both turbulence and surface roughness. **Lift (c_l) and drag (c_d) coefficients are measured to determine whether the proposed passive approach can**

mitigate the adverse aerodynamic effects induced by these combined perturbations.

The remainder of this paper is organized as follows. SEC. II describes the experimental setup and methodology adopted for the tests. SEC. III presents and analyses the aerodynamic results obtained under the different flow paradigms. Finally, SEC. IV summarises the main conclusions and discusses future directions for research on passive flow control in realistic transitional regimes.

II. RESEARCH FRAMEWORK

The research follows a single, experimentally based workflow aimed at characterising the aerodynamic behaviour of a NACA0021 airfoil equipped with passive devices (*PD*s) under different flow conditions. The study focuses exclusively on the airfoil scale, where the combined effects of turbulence and surface roughness can be isolated, quantified, and compared against the baseline clean flow. SUBSEC. II A describes the experimental facility, the measurement procedures, and the range of conditions explored.

A. Experimental methodology

1. Wind-tunnel setup

Experiments were carried out in an open-circuit, low-turbulence wind tunnel driven by a 37 kW fan. The test section has a rectangular cross-section of 0.75×1 m^2 and a length of 3 m, allowing freestream velocities up to 40 m/s with background turbulence levels below 0.2%. Further information on the facility and its flow quality parameters can be found in[53,54]. A schematic of the experimental arrangement is shown in FIG. 1a.

The NACA0021 airfoil was selected as the test geometry for several reasons.

1. First, it is a symmetric, non-cambered profile, which facilitates interpretation of aerodynamic data by eliminating geometric bias between positive and negative angles of attack.
2. Second, its simple analytical definition and public availability enable direct comparison with a large body of experimental and computational studies spanning the transitional Reynolds-number range[8,10,12].
3. Third, the NACA0021 has become a reference configuration for flow-control investigations[49,51,52], offering an established aerodynamic baseline and a robust validation framework for assessing the effects of surface-mounted devices.

Altogether, these characteristics make the NACA0021 an attractive canonical configuration for investigating the mechanisms through which turbulence, surface roughness, and passive control strategies interact. More generally, airfoils of the NACA family satisfy several desiderata that make them convenient benchmark geometries: their analytic definition ensures geometric reproducibility, their aerodynamic behavior has been widely documented, and extensive comparative data are available across a broad range of flow conditions.

The particular case study considered herein corresponds to a specific experimental realization of such a geometry. The prototype consists of an extruded, spanwise-homogeneous profile with chord $c = 0.15$ m and span $s = 0.30$ m, yielding an aspect ratio $AR = 2$. For completeness, the leading-edge geometric scale is also noted: for the NACA0021 profile the classical formulation gives $r_{\mathrm{LE}} \approx 0.0486 \cdot c$, corresponding to a characteristic diameter $d_{\mathrm{LE}} \approx 0.097 \cdot c$ (≈ 14.6 mm for the present model). While this geometric scale is known to influence transitional boundary-layer behavior and separation sensitivity, the airfoil geometry is kept fixed in the present study, which instead focuses on the effects of externally imposed perturbations.

The *PD*s consist of triangular stripes with a side length of $l = 13$ mm and a height of $h = 1$ mm, periodically distributed along the span. The fast-computing viscous–inviscid coupled code XFOIL[55] has been employed to estimate the boundary-layer momentum thickness θ and to compare it with the height of the roughness elements through the ratio h/θ. The results show that, in the mid-chord region where the elements are located, $h/\theta = \mathscr{O}(10)$. Although this metric indicates that the height of the elements is significantly larger than the local boundary-layer thickness, it is intentionally chosen to ensure that the induced perturbation is sufficiently energetic. Because the element height h is an order of magnitude larger than the corresponding momentum thicknesses, these elements protrude into the freestream and act as macro-geometric vortex generators rather than classical intra-layer boundary-layer trips.

Nevertheless, it is to recall that the goal is not to reproduce a realistic surface roughness, but to introduce a controlled disturbance capable of modifying the near-wall momentum distribution and promoting vortex generation. The suitability of the XFOIL-based estimations will be discussed in light of the c_p distributions presented later (see FIG. 2 and 3). This scaling approach follows that adopted in similar low-Reynolds-number studies[14,39,40], in which exaggerated geometrical features are used to amplify boundary-layer responses above the experimental uncertainty threshold.

The distance between adjacent elements equals their side length ($r = l$), maintaining uniform spacing and ensuring a quasi-two-dimensional perturbation field. The only variable parameter is the non-dimensional chordwise location of the device line, defined as x/c. Two positions were tested: $x/c = 0.25$ (*PD25*) and $x/c = 0.5$ (*PD50*); configurations without devices are referred to as *Bare* cases. The relevant parameters of the employed airfoil prototype and the discrete roughness elements are gathered in TABLE I.

The freestream velocity was measured using a *Delta-Ohm HD49047T01L* Pitot–static probe (full-scale range 41.75 m/s), operated at a sampling frequency of 100 Hz. Its resolution (0.0012% FS $\approx 5 \times 10^{-3}$ m/s) and accuracy (± 1% FS) ensured adequate sensitivity under the present low-

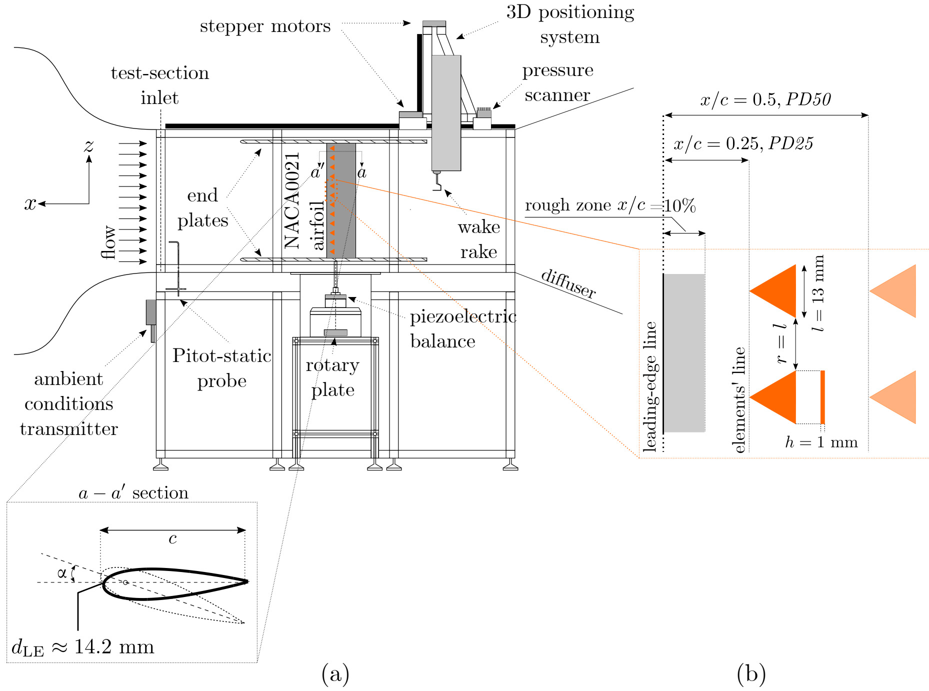

FIG. 1: (a) Wind-tunnel setup used for testing the NACA0021 airfoil equipped with passive devices (*PD*s). (b) Generic distribution of the *PD*s on the airfoil surface.

TABLE I: geometrical parameters of the employed airfoil and discrete roughness elements.

Airfoil geometry	NACA0021
c	0.15 m
s	0.3 m
AR	2
d_{LE}	14.2 mm
Roughness geometry	**Equilateral triangle**
l	13 mm
h	1 mm
r	13 mm
x/c	$[0.25, 0.5]$

Reynolds-number conditions. Ambient pressure and temperature were monitored using a *Delta-Ohm HD*2001.1 transmitter, also sampled at 100 Hz. The device provides a pressure full-scale range of 600–1100 mbar, with resolution 0.01% FS $\approx$ 0.05 mbar and accuracy $\pm$0.1% FS, and a temperature full-scale range of -20–80°C with resolution (0.05% FS and accuracy $\pm$0.3°C, ensuring accurate density corrections throughout the campaign.

Unlike previous studies by the authors that employ the same experimental set-up for airfoil characterization[15,17], the measurements carried out herein are restricted to lift and drag forces. In the studies mentioned above, the experimental campaign comprised both global (lift/drag) and local (c_p distributions and oil-flow visualizations) measurements under the *Clean* flow paradigm. However, the authors have found that the local measurements obtained under the other flow conditions are not directly applicable to the other flow paradigms, mainly due to the unsteady flow features introduced by turbulence and roughness effects. Although ongoing research is being conducted to devise refined experimental procedures that allow undertaking such measurements, the current technical capabilities lie exclusively on the side of the global parameters.

As such, lift forces were measured using a *Kistler 9119AA2* piezoelectric balance sampled at 500 Hz. The balance offers a maximum full-scale range of $\pm$4 kN, a resolution of 2 mN, and natural frequencies above 6 kHz, providing high fidelity for steady aerodynamic-load measurements. Drag was obtained from the momentum-deficit method[56] using an *Aerolab* wake rake connected to a *Scanivalve MPS4264* differentialpressure scanner. The scanner, operated at 750 Hz, features a full-scale range of ± 1000 Pa with accuracy $\pm 0.15\%$ FS $\approx \pm 1.5$ Pa and sufficiently high dynamic response for resolving wake-pressure distributions.

For each flow configuration and angle-of-attack setting, measurements were acquired over 30 s to ensure statistical convergence of forces and pressures. After each angular adjustment, the flow was allowed to stabilise for 10 s before data acquisition commenced. All sensors were integrated into a *National Instruments* data-acquisition system and monitored through a custom LABVIEW interface[57].

2. Flow conditions

Two flow paradigms were considered:

1. a *Clean* flow corresponding to the default low-turbulence tunnel condition, and
2. a *Combined* flow considering both controlled turbulence and surface roughness.

A passive grid installed at the inlet of the test section generated a turbulent field with an intensity of approximately $I = 3.8 \pm 0.2\%$ and an integral-lenghtscale-to-chord-ratio of $\ell/c = 0.25 \pm 0.05$[15,17]. Although the intensity value is below those commonly encountered in urban or complex-terrain environments[58], it is representative of moderate, well-characterized turbulence conditions suitable for controlled laboratory testing. Higher intensities would compromise repeatability and violate the self-similarity assumptions required by Kolmogorov's decay law. The condition $\ell/c = \mathscr{O}(1)$ is relevant, as it indicates that the dominant turbulent length scales are of the same order as the chord and may therefore exert a significant influence on the airfoil aerodynamics. Surface degradation was emulated by applying a 0.5 mm height band of P80-grade sandpaper showing a mean grain height of ≈ 100 μm to 10% of the chord around the leading edge (both at pressure and suction sides), following the methodology in[28]. In the vicinity of the leading-edge, XFOIL-based θ estimations provide $k/\theta = \mathscr{O}(1)$, indicating that the sandpaper is liable to trip the boundary-layer and cause a bypass transition. These two perturbations were joined in the *Combined* configuration to reproduce realistic, environmentally disturbed aerodynamic conditions.

Experiments were performed at three chord-based Reynolds numbers within the transitional range, $\mathrm{Re} = [0.8, 1.0, 1.2] \times 10^5$. For each condition, the lift and drag coefficients (c_l, c_d) were measured over a cyclic angle-of-attack loop. The increasing branch covered $\alpha \in [0^\circ, 20^\circ]$ in 1° increments, and the decreasing branch retracted the same range ($\Delta\alpha = -1^\circ$), enabling capture of the aerodynamic hysteresis associated with stall and reattachment[8]. The complete test matrix is summarized in TABLE II.

3. Uncertainty analysis

Each test case was repeated three times to ensure statistical repeatability. For each repetition, the full Reynolds-number sweep of the campaign was completed and the corresponding angle-of-attack route was performed at every Reynolds number. Between repetitions, the airfoil prototype was intentionally dismounted and reinstalled on the rotary plate/balance assembly. This procedure allows run-to-run variability associated with model installation—such as small differences in positioning, alignment, and tightening/preload conditions of the mounting interface—to contribute to the overall repeatability assessment. In this manner, the reported dispersion encompasses not only the intrinsic variability of the measurement chain but also the additional uncertainty introduced by the practical handling of the prototype within the test section.

The datasets presented in SEC. III correspond to the mean values of the three trials. Uncertainty bounds were computed using a first-order (linear) propagation scheme detailed in previous works by the authors[54,59], which is based on the propagation of uncertainties from the basic measurands of the experiment to the derived quantities (i.e. c_l and c_d) through the framework originally proposed by Kline and McClintock[60]. All reported intervals correspond to a 95% confidence level. As will become clear when presenting the results in SEC. III, the uncertainty values are not overlaid on the figures as error bars or shaded bands for avoiding an excessive cluttering of the plots; instead, the maximum, mean, and standard deviation of the resulting uncertainties in c_l and c_d are reported in TABLE III.

III. RESULTS AND DISCUSSION

A. Aerodynamic behaviour analysis

This section examines how the NACA0021 airfoil responds to the two considered flow paradigms—*Clean* and *Combined* (turbulence plus leading-edge roughness)—and to the different passive-device (*PD*) layouts. The analysis is based on global aerodynamic quantities: lift coefficient c_l, efficiency $E = c_l/c_d$, and stall angle α_{stall}.

FIG. 4-FIG. 6-FIG. 8 present the c_l–α and E–α curves for all configurations under both *Clean* and *Combined* conditions at the three tested Reynolds numbers. FIG. 5-FIG. 7-FIG. 9 focus exclusively on the *Combined* cases to highlight the relative effect of *PD25* and *PD50*. Finally, FIG. 10 summarizes the key indicators ($c_{l,\max}$, $E_{\max}$, α_{stall}) and helps to interpret the global trends. As mentioned in SEC. II, the aerodynamic polars were acquired through a cyclic angular route in order to capture possible hysteresis effects associated with stall. In the pre-stall region, where the forward- and backward-route measurements were found to coincide within the experimental scatter, a single data point is reported for each angle of attack (i.e., the two branches are collapsed into one) to avoid redundant information. Conversely, in the vicinity of stall and in the post-stall regime, where hysteresis may be present, the forward and backward branches are retained as acquired so

TABLE II: parametrical schedule for the experimental testing campaign.

Flow paradigm	Reynolds number	Angular config.	Elements' chordwise position, x/c	# cases
Clean	$\mathrm{Re} \in [0.8, 1, 1.2] \cdot 10^5$	$\alpha \in [0, 20]^\circ$, $\Delta\alpha = 1^\circ$ $\cup$ $\alpha \in [20, 0]^\circ$, $\Delta\alpha = -1^\circ$	*Bare*, 0.25, 0.5	9
Combined				9
				Total 18

TABLE III: maximum, mean and standard deviations of the uncertainty intervals.

Flow paradigm	c_l−related			c_d−related		
	$\delta_{c_{l_{max.}}}$	$\overline{\delta_{c_l}}$	$\sigma_{\delta_{c_l}}$	$\delta_{c_{d_{max.}}}$	$\overline{\delta_{c_d}}$	$\sigma_{\delta_{c_d}}$
Clean	0.1676	0.1523	7.14×10^{-3}	5.27×10^{-2}	2.42×10^{-2}	1.55×10^{-2}
Combined	0.1595	0.1569	3.11×10^{-3}	0.1371	5.09×10^{-2}	3.13×10^{-2}

that the loop behaviour is explicitly represented.

To improve plot readability, distinct colour codes are used for the *Clean* and *Combined* datasets. Symbols and line styles are assigned according to the test Reynolds number: the circular–solid, triangular–dashed and square–dotted marker–line pairs correspond to the $[0.8, 1, 1.2] \cdot 10^5$ cases, respectively. For the *Combined* dataset, hollow markers are employed to further enhance readability. Whenever specific features of the curves need to be emphasized, the relevant regions are highlighted using annotations and shaded areas.

To make the discussion clear and readable, the results are organized as follows:

1. description of the main trends at each Reynolds number,
2. cross-comparison of the influence of the *PD*s and flow conditions, and
3. a compact physical interpretation using simple, mechanism-based arguments.

Before entering the discussion itself, and for the sake of facilitating the interpretations regarding the LSB behavior under different flow paradigms, it is considered necessary to present some local c_p distributions and oil-flow visualizations carried out by the authors upon the same airfoil geometry, and which have been published in a previous study[15]. Those c_p − vis. correlations are intended to shed light on the understanding of the laminar-to-turbulent transition, and to provide the conceptual tools for understanding the evolution of the global parameters (i.e. c_l and E) on the basis of such a framework. As expressed in SUBSEC. II A 1, a number of technical limitations hinder the possibility to extend those measurements to the overall set of flow paradigms. Nevertheless, it is considered that the local-global correlations are sound enough as to extend the explanatory framework proposed in previous analyses[15] to the current study.

FIG. 2 and 3 present the c_p–visualization correlations discussed above. In particular, FIG. 2 illustrates how the laminar–turbulent transition evolves with increasing angle of attack α, with vertical lines indicating the onset and closure of the laminar separation bubble (LSB).

Based on the qualitative information obtained from the oil-flow visualizations, the onset of the LSB can be associated with the chordwise location where streaks of painted oil first become visible. Upstream of this point, the boundary layer remains laminar and sweeps the oil away from the surface. The unperturbed painted region located between the vertical lines for each angular configuration corresponds to the spatial extent of the bubble. This region can be correlated with the nearly constant pressure distribution observed in the corresponding c_p plots.

Downstream of the closure line—identified by a sudden reattachment—the boundary layer becomes turbulent and the airfoil surface is again swept by the flow. Near the trailing edge, the combined effect of the airfoil's vertical orientation in the wind-tunnel test section and the accumulation of oil near the edge causes gravity-induced downward streaks before the final flow detachment occurs. As shown in the visualizations, this trailing-edge detachment progressively shifts toward the leading edge as α increases. Besides, an XFOIL-based c_p curve has been plotted for the $\mathrm{Re} = 1.2 \cdot 10^5$ case. The prediction exhibits a slightly less abrupt reattachment and somewhat higher pressure levels along the pressure side; nevertheless, the overall correspondence with the experimental distribution remains acceptable. Overall, an increase in α is shown to cause a shrinking of the LSB and its forward motion.

FIG. 3 shows the effect of the Reynolds number for a given incidence angle of the flow (i.e. 6°). The Reynolds number dependency, or the so-called scale-effect, is manifested as a shortening of the bubble with increasing flow velocity, which is the parameter that determines the Reynolds number in the test. As observed, the average location of the LSB does not seem largely affected, but its extent drops from $\approx 0.3\cdot c$ to $0.18\cdot c$ when doubling the Reynolds number in the range $\mathrm{Re} \in [0.8, 1.6]\cdot 10^5$. Notice that the Reynolds interval covered in FIG. 3 is wider than the one proposed in the current study. This is due to the fact that the inclusion of passive grids for turbulence generation induce a severe choking within the test-section, requesting a higher fan power for achieving the same flow velocity. Due to safety reasons, the limited power of the fan does not enable to surpass the threshold of $\mathrm{Re} = 1.2\cdot 10^5$ when turbulent configurations are reproduced, constraining the experimental campaign accordingly.

The reduction of the pressure plateau is also evident in the c_p distributions, and the lowering of the pressure initial pressure peak as well, together with the less pronounced gradients that correspond to the reattachment phenomenon. The flow detachment observed near the trailing edge becomes less pronounced as the Reynolds number increases. This behavior can be attributed to the higher freestream velocity, which energizes the turbulent boundary layer and enhances its ability to withstand the adverse pressure gradient, thereby delaying or reducing the extent of separation. Here as well, the XFOIL-based curves that have been plotted for the $\alpha \in [3, 6, 9]^\circ$ cases to avoid excessive clutter in the figure, provide clear support for the θ estimations reported in SUBSEC. II A 1. With all, an increase in Reynolds number correlates with a shorter bubble extent, its onset displacing downstream and the reattachment mechanism moving towards the leading-edge, which redounds to larger coverages of both the laminar and the turbulent boundary-layers. The mechanisms described above, present in both FIG. 2 and 3, must be considered when interpreting the results that follow.

Case $\mathrm{Re} = \mathbf{0.8 \times 10^5}$:

Clean baseline and laminar-separation-bubble effects. At $\mathrm{Re} = 0.8 \times 10^5$ the flow is strongly transitional and highly sensitive to any external disturbance or surface modification. In the *Clean Bare* configuration (FIG. 4a), the lift curve c_l–α is nearly linear only at very low incidence, before departing from linearity at around $\alpha \approx 3^\circ$. This behaviour is typical of low-Reynolds-number symmetric airfoils and stems from the formation of a laminar separation bubble (LSB) near the leading edge. As mentioned above, when the laminar boundary layer encounters an adverse pressure gradient, it separates, transitions to turbulence within the separated shear layer, and reattaches further downstream. This process alters the effective camber of the airfoil and distorts the ideal linear lift response[8,51].

As mentioned before, when α increases the bubble shrinks and moves towards the leading-edge while sustaining a relatively high c_l value in the pre-stall region. Eventually, the bubble is unable to sustain the large pressure-gradient in the vicinity of the leading-edge, and undergoes a bursting phenomenon whereby a sharp stall is observed in the experimental curves, with the overall boundary-layer turning turbulent after stalling. In the pre-stall region, the reattachment of the flow downstream the LSB closure is followed by the development of a turbulent boundary-layer and its definite detachment near the trailing-edge. It has been shown that the onset of such a detachment shifts towards the leading-edge, and it contributes to the saturation of the lift value before the bursting occurs. As discussed previously, the combined mechanism of the LSB formation and the trailing-edge detachment sensibly depends on Re apart from α. Indeed, the lower the Reynolds number, the stronger the laminar nature of the boundary-layer and, consequently, the larger the generated LSB and its potential effect[15,17]. However, as mentioned in SUBSEC. II A 1, such local correlations are not directly applicable to flow paradigms other than the *Clean* one, which is the reason why the analysis that follows relies exclusively on global parameters. Nevertheless, this does not imply that certain features related to the LSB and stalling behavior observed in the local trends[15] cannot be extrapolated, with all the careful considerations required, to the explanatory framework of other flow paradigms.

Effect of the Combined flow paradigm. Introducing the *Combined* flow paradigm—where controlled turbulence and leading-edge roughness coexist—fundamentally alters the aerodynamic response. The c_l–α curve becomes more linear over a broader range of angles, indicating that the combined disturbances promote earlier transition and suppress or shorten the LSB[8,16]. However, the slope of this quasi-linear region is lower, and the maximum lift coefficient decreases. Physically, while the flow becomes more predictable and the drop in c_l is less abrupt when the airfoil stalls, the boundary layer thickens due to its inherent turbulent nature (promoted either by the incoming flow's turbulence or by the roughness-induced bypass transition, or both) and, consequently, the viscous losses rise, inducing the observed drops in E. Likewise, and given that a turbulent boundary-layer is able to sustain larger pressure gradients, the stalling phenomenon is correlatively delayed[15]. The resulting behavior is therefore smoother in terms of stall onset and c_l drop, but less aerodynamically efficient.

Role of passive-device layouts. Adding *PD*s on one side of the airfoil introduces a distinct lift offset at $\alpha = 0^\circ$. The *PD25* layout produces a negative offset, while *PD50* yields a positive one. This is a purely geometric effect: unilateral surface modification breaks the symmetry of the NACA0021 profile, shifting the stagnation point and introducing an effective camber. Offsets appear under both *Clean* and *Combined* conditions, although they are milder under the latter due to increased mixing and reduced sensitivity to small geometric asymmetries[16]. Under *Clean* flow conditions, these offsets vanish as α increases and the flow approaches saturation, since the global dynamics are dominated by bubble growth and stall. In contrast, the more linear *Combined* cases preserve a residual offset across a wider range of angles, as the stabilized boundary layer transmits the asymmetry more effectively.

The effect of *PD*s on stall behaviour is closely tied to their placement along the chord and the prevailing boundary-layer state. Under *Clean* inflow, *PD25* acts as an early trip that energises the boundary layer before natural separation. This enhances the momentum near the wall, allowing the flow to

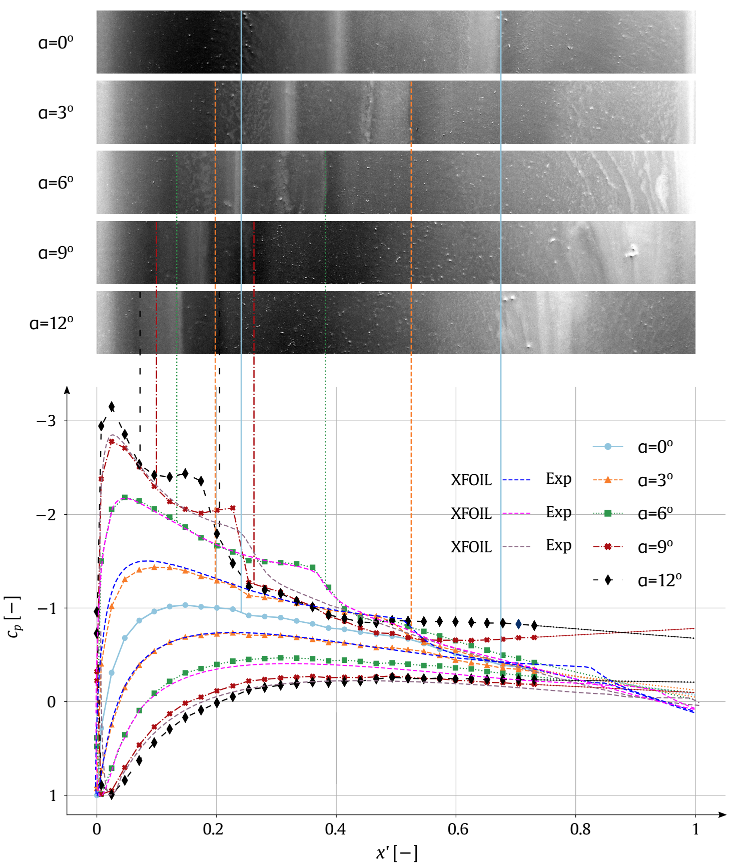

FIG. 2: c_p distributions and oil-painting-based flow-visualizations performed for a NACA0021 airfoil tested at several angles-of-attack and $\mathrm{Re} = 1.2{\cdot}10^5$. Reprinted from Measurement 188 (2022), A. Zarketa-Astigarraga, M. Penalba, A. Martin-Mayor, M. Martinez-Agirre, Experimental assessment of scale-effects on the aerodynamic characterization of a transitionally-operating airfoil working under clean flow conditions, Copyright 2022 with permission from Elsevier.

resist adverse pressure gradients and delaying stall. In contrast, *PD50* sits closer to the natural separation point, where the flow is already unstable or partially detached; here, the device mostly adds form drag and can even promote earlier stall. Under *Combined* inflow, the boundary layer is already turbulent over much of the chord, so the additional perturbation from either *PD* configuration exerts a weaker influence on α_{stall}. The devices then behave less as tripping mechanisms and more as minor roughness elements.

Impact on aerodynamic efficiency. The corresponding efficiency curves (FIG. 4b) summarise these behaviours. For *Clean* conditions, *PD50* shows a modest efficiency improvement at low α, implying that, in a narrow operational range, the mid-chord elements enhance mixing or reduce drag slightly without compromising lift. However, this advantage disappears as the flow approaches stall. Conversely, *PD25* yields a noticeable efficiency gain at higher α, where its stall-delay effect leads to higher $E = c_l/c_d$ values compared to the *Bare* airfoil. Under *Combined* flow, all configurations exhibit significantly lower efficiency—reductions of 30% or more for comparable angles-of-attack—because the beneficial effects of bubble suppression and smoother stall are offset by higher viscous and form drag. Overall, in this low-Re transitional regime, the interaction between flow disturbances and passive devices is highly delicate: small geometric interventions can bring local improvements, yet the prevailing trend under realistic inflow is a net reduction in aerodynamic efficiency.

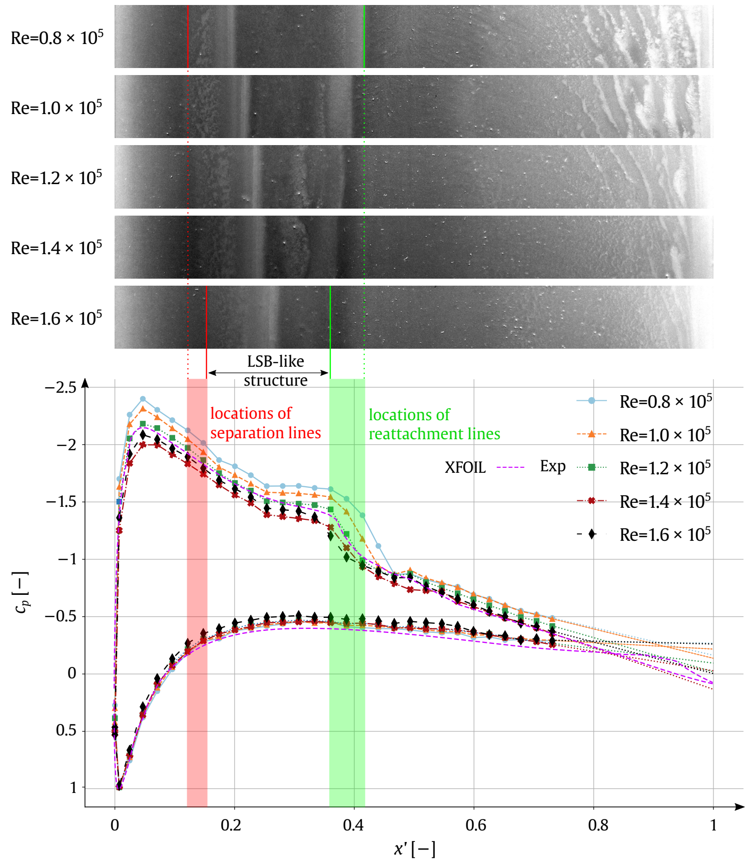

FIG. 3: c_p distributions and oil-painting-based flow-visualizations performed for a NACA0021 airfoil tested at several Reynolds numbers and at a $\alpha = 6°$. Reprinted from Measurement 188 (2022), A. Zarketa-Astigarraga, M. Penalba, A. Martin-Mayor, M. Martinez-Agirre, Experimental assessment of scale-effects on the aerodynamic characterization of a transitionally-operating airfoil working under clean flow conditions, Copyright 2022 with permission from Elsevier.

Case $\mathrm{Re} = \mathbf{1.0 \times 10^5}$:

Clean baseline. At $\mathrm{Re} = 1.0 \times 10^5$ the same mechanisms remain, but their relative importance changes as the boundary-layer becomes thinner and less laminar, as shown when discussing FIG. 2 and 3 and corroborated in previous studies[15,51]. In fact, the LSB extent has been shown to reduce, on average, between $5-7\%$ of the chordal length when compared to its lower-Re counterpart[15]. In the *Clean* cases (FIG. 6a), the lift curves remain almost linear over a wider α range than at $\mathrm{Re} = 0.8 \times 10^5$. LSBs are smaller and less influential, and transition occurs earlier along the chord. Likewise, the trailing-edge detachment is not as effective in contributing to c_l saturation, and relatively higher lift coefficient values are achieved. As a result, the $c_l - \alpha$ curves stand above their lower-Re counterparts, stall is sensibly delayed and the c_l drop observed thereof is less abrupt. The three *Clean* configurations (*Bare*, *PD25*, and *PD50*) converge to similar maximum lift and stall angles, showing that once the boundary layer is mostly turbulent before separation, the passive devices exert limited influence[8].

Effect of the Combined flow. Under *Combined* conditions (FIG. 7a), the interplay between turbulence, surface roughness, and *PD* placement becomes more nuanced. A distinct lift enhancement appears for *PD50* over a finite range of angles, where it outperforms both the *Bare* and *PD25* configurations. At this Reynolds number, the discrete mid-chord elements act as macroscopic, three-dimensional vortex generators. Because their height ($h = 1$ mm) protrudes into the

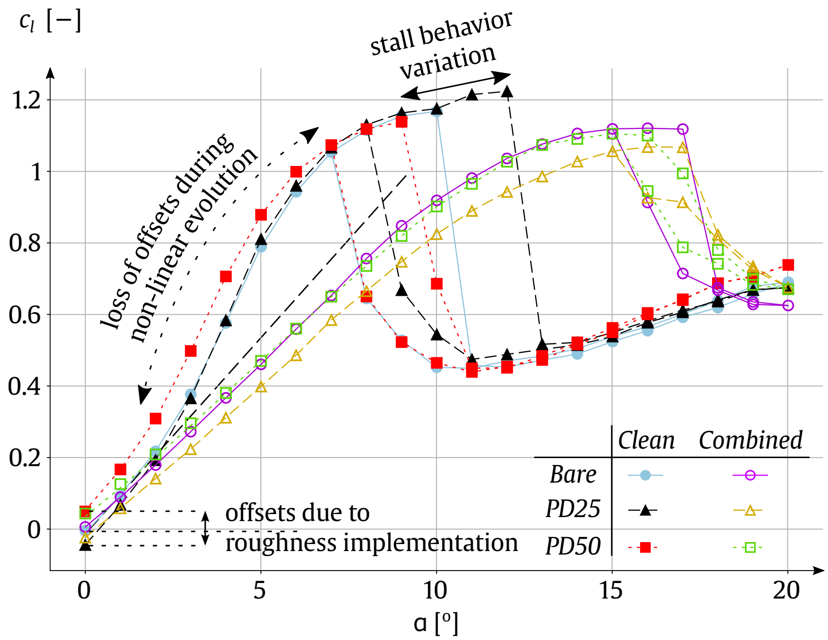

(a) $c_l - \alpha$ curves

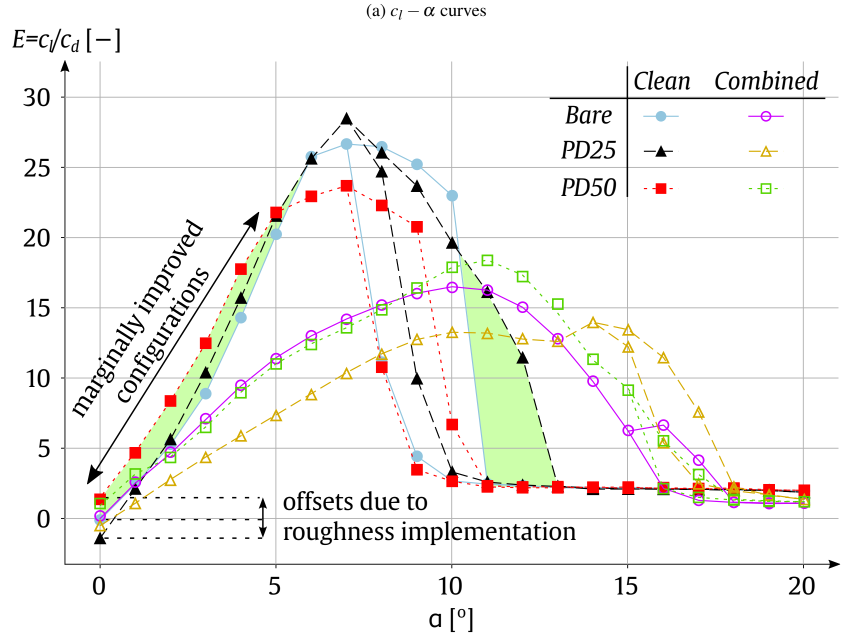

(b) $E - \alpha$ curves

FIG. 4: Characteristic curves for *Clean* and *Combined* flow paradigms with different *PD* configurations at $\mathrm{Re} = 0.8 \times 10^5$.

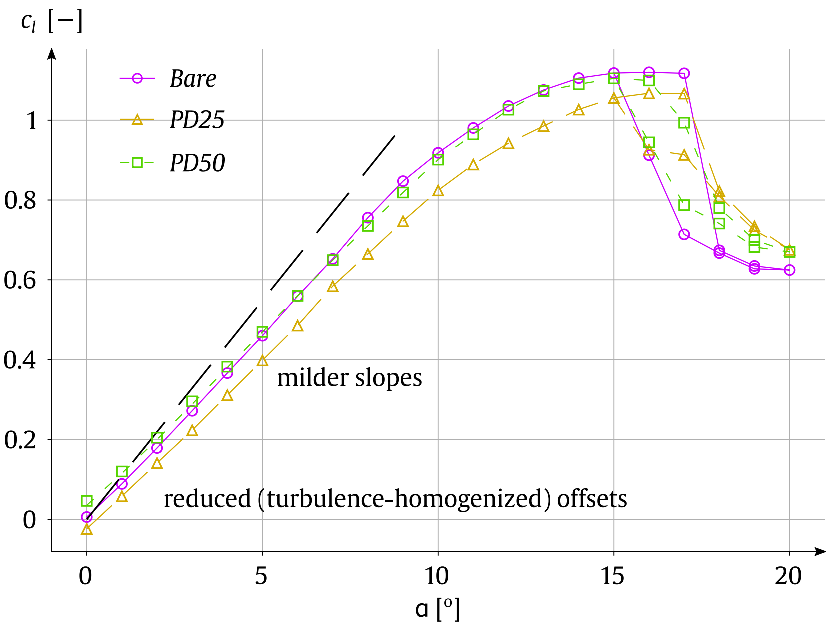

(a) $c_l - \alpha$ curves

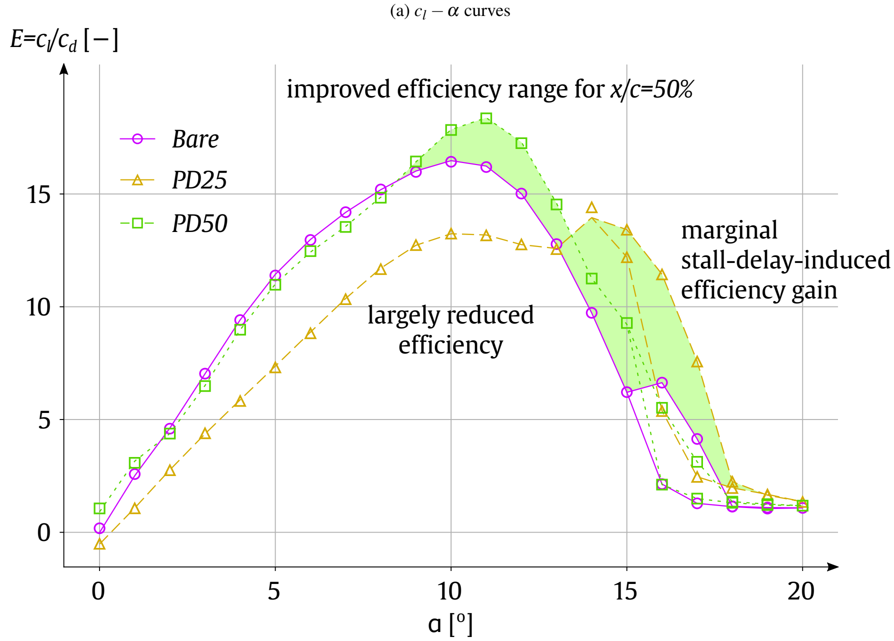

(b) $E - \alpha$ curves

FIG. 5: Characteristic curves under *Combined* flow conditions with different *PD* configurations at $\mathrm{Re} = 0.8 \times 10^5$.

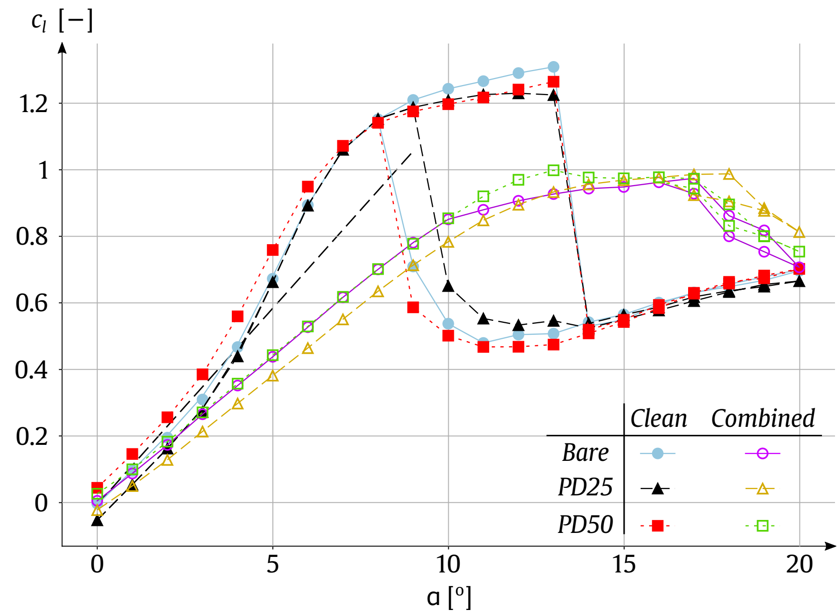

(a) $c_l - \alpha$ curves.

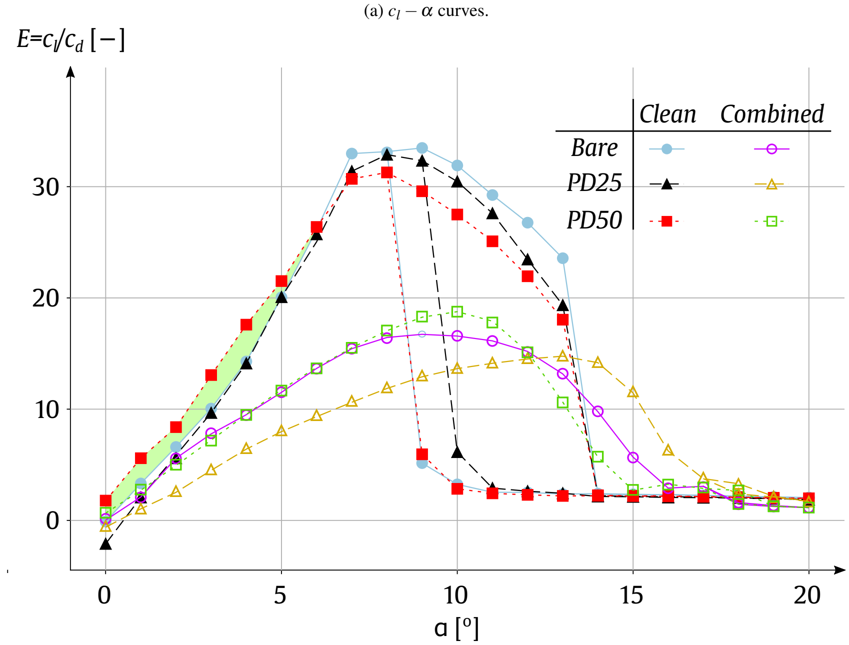

(b) $E - \alpha$ curves.

FIG. 6: Characteristic curves for *Clean* and *Combined* flow paradigms with different *PD* configurations at $\mathrm{Re} = 1 \times 10^5$.

higher-velocity flow, they shed streamwise trailing vortices. As described in classical studies of imbedded longitudinal vortices[61,62], these vortical structures induce a strong downwash motion that actively entrains high-momentum fluid from the freestream into the decelerated near-wall region. This forced momentum exchange re-energizes the boundary layer, accelerating the local transition to turbulence and leading to a forced and stable reattachment mechanism that bypasses the natural amplification of 2D separated-flow instabilities.

Effect of passive devices and efficiency. The efficiency results (FIG. 6b) mirror the lift behaviour. In *Clean* inflow, both *PD25* and *PD50* drop below the *Bare* case beyond $\alpha \approx 6^{\circ}$, as the additional drag from the devices outweighs any benefit. In *Combined* inflow (FIG. 7b), *PD50* maintains a slight efficiency increase in the same angular range where it lifts performance, while *PD25* provides only marginal improvements linked to modest stall delay. Hence, at $\mathrm{Re} = 1.0 \times 10^5$, the positive effects of passive devices persist but become narrowly limited to specific geometries and angles-of-attack.

Case $\mathrm{Re} = \mathbf{1.2 \times 10^5}$:

Clean baseline. For $\mathrm{Re} = 1.2 \times 10^5$, the boundary layer develops an even shorter LSB, shrinking its extent an additional 5% of the chord compared to its lower-Re counterpart[15], as shown in FIG. 3. The $c_l - \alpha$ curves (FIG. 8a) display a broad linear region up to $\alpha \approx$ 5–6°, followed by a brief non-linear zone and stall. Maximum lift and stall angles are nearly identical among all *Clean* configurations, indicating minimal influence from the passive devices. Here, *PD25* slightly flattens the post-linear region and causes an earlier stall, showing that at higher Re, the same trip becomes primarily a drag-inducing roughness element rather than an effective flow-control device.

Effect of the Combined flow. The *Combined* results (FIG. 9a) highlight a sharper contrast between the two layouts. *PD50* rapidly loses its initial lift offset and reaches the lowest $c_{l,\max}$, confirming that mid-chord elements mostly thicken the wake and penalise lift once the boundary layer is already turbulent and rough. By contrast, *PD25* sustains higher lift at large α and even surpasses the *Bare Combined* case at high incidence. At this stage, the leading-edge devices function as effective vortex generators, delaying separation and preserving lift despite the disturbed inflow.

Efficiency and practical implications. As seen in FIG. 8b and FIG. 9b, these effects translate directly into the efficiency curves. In *Clean* inflow, neither configuration improves performance: the boundary layer is too thin, and the device height is relatively large, increasing total drag. Under *Combined* inflow, efficiency losses exceed 60% compared with the *Clean* baseline[16]. Nevertheless, *PD25* recovers a noticeable E improvement at high α due to its stall-delay effect, while *PD50* remains detrimental across most of the operational range.

Global synthesis and physical interpretation

FIG. 10 summarises the behaviour of all configurations:

- *Maximum lift* ($c_{l,\max}$, FIG. 10a)): for all Re, *Combined* conditions reduce $c_{l,\max}$ with respect to the *Clean Bare* reference, with losses that can exceed 30%. The influence of *PD25* and *PD50* on $c_{l,\max}$ is not uniform: small improvements appear only in restricted cases, while in many others the devices are neutral or detrimental.

- *Maximum efficiency* ($E_{\max}$, FIG. 10b)): the degradation of efficiency is even stronger. In the most unfavourable *Combined* scenarios and highest Re, $E_{\max}$ reductions approach 70% compared to the *Clean* baseline. *PD25* provides clear benefits only at low Re or at high α under *Combined* flow; *PD50* offers local gains at intermediate Re in *Combined* conditions but becomes clearly unfavourable at $\mathrm{Re} = 1.2 \times 10^5$.

- *Stall angle* (α_{stall}, FIG. 10c)): *Combined* conditions generally increase α_{stall} with respect to *Clean*, as the more energetic (partly turbulent) boundary layer tolerates stronger adverse pressure gradients before detaching[8]. *PD25* can further delay stall in several configurations, whereas *PD50* tends to either promote slightly earlier stall or leave it nearly unchanged.

These results can be understood in terms of three simple mechanisms:

1. *Laminar separation bubble control.* Turbulence and leading-edge roughness shrink or remove the LSB. This makes lift curves smoother and reduces hysteresis, but lowers the lift slope and increases drag. The flow becomes more stable but less aerodynamically efficient.

2. *Position of the passive devices.* Devices at $x/c = 0.25$ act near the natural separation and transition region. When the flow is still partly laminar, they can energise the boundary layer and delay stall (beneficial at low Re or high α in *Combined* flow). Devices at $x/c = 0.5$ interact mostly with an already separated or turbulent layer; in many cases, they add form drag without significantly improving attachment.

3. *Increase of* Re*.* As Re increases, the boundary layer becomes thinner and more turbulent. The fixed-height devices effectively become taller relative to the boundary layer thickness, and their action turns more intrusive. The range of conditions where such passive elements are beneficial becomes narrower, and at the highest tested Re they are often counterproductive unless very specifically placed.

Finally, it is worth noting that this study is based on global force measurements. These are well suited for quantifying the net impact of turbulence, roughness, and *PD* layouts on performance, but they do not resolve all details of the flow physics. Previous work for *Clean* conditions[8] has shown that local measurements (pressure distributions, flow visualizations, or velocity field measurements) provide valuable additional insight. Extending such local techniques to the present *Combined* configurations, with and without *PD*s, is a natural continuation of this research.

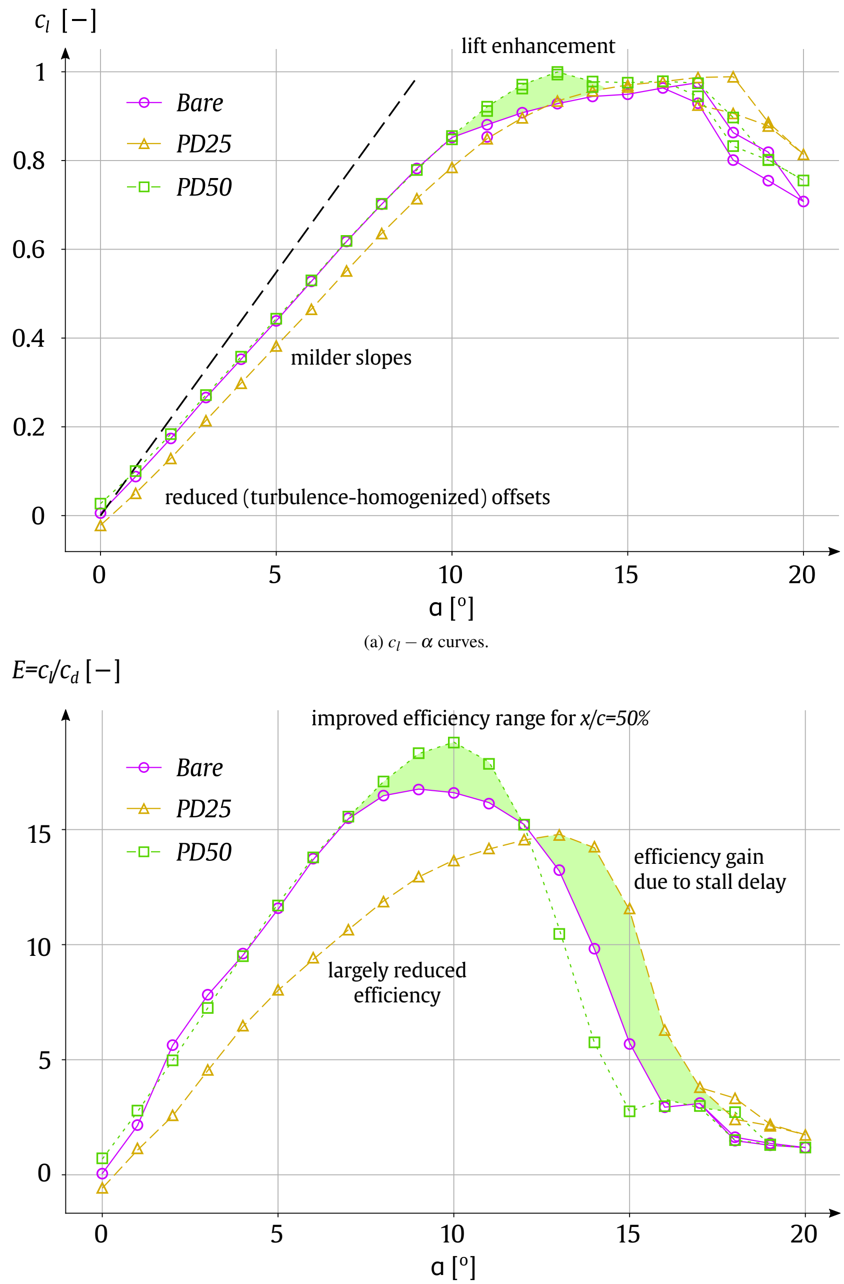

(a) $c_l - \alpha$ curves.

(b) $E - \alpha$ curves,

FIG. 7: Characteristic curves under *Combined* flow conditions with different *PD* configurations at $\mathrm{Re} = 1 \times 10^5$.

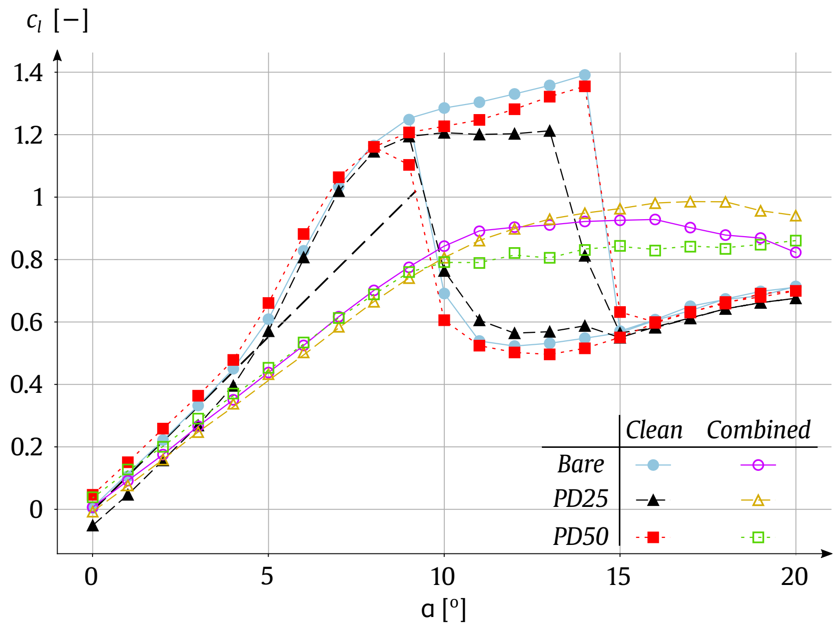

(a) $c_l - \alpha$ curves

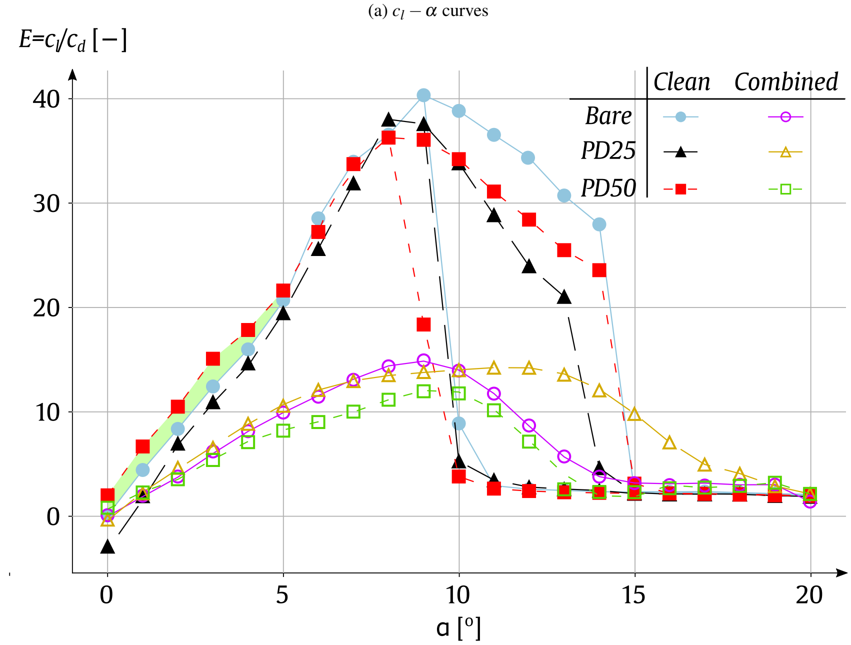

(b) $E - \alpha$ curves

FIG. 8: Characteristic curves for *Clean* and *Combined* flow paradigms with different *PD* configurations at $\mathrm{Re} = 1.2 \times 10^5$.

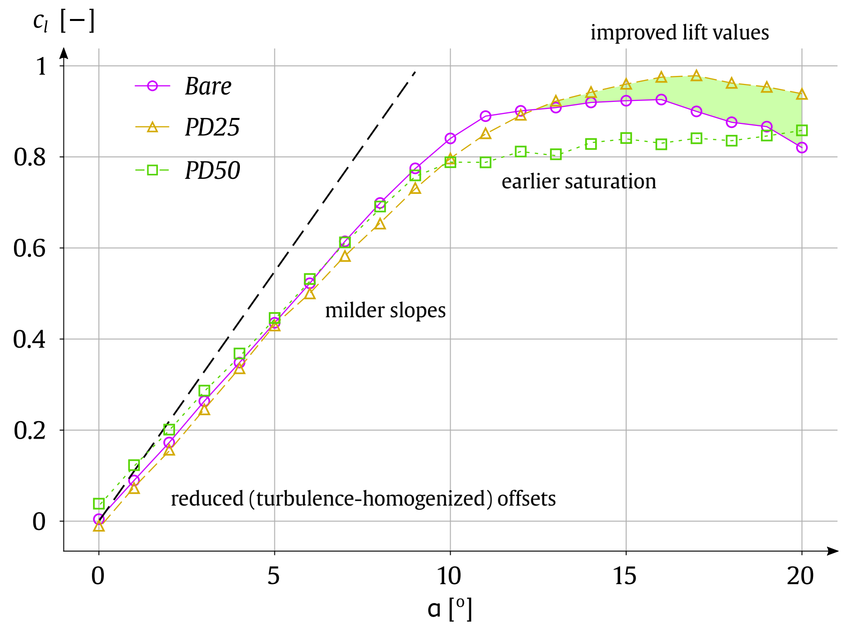

(a) $c_l - \alpha$ curves

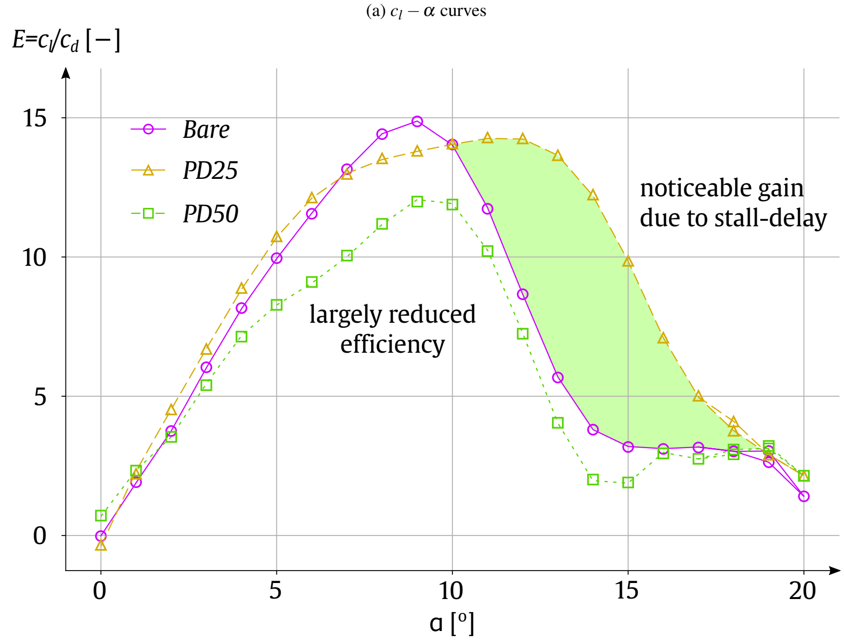

(b) $E - \alpha$ curves

FIG. 9: Characteristic curves under *Combined* flow conditions with different *PD* configurations at $\mathrm{Re} = 1.2 \times 10^5$.

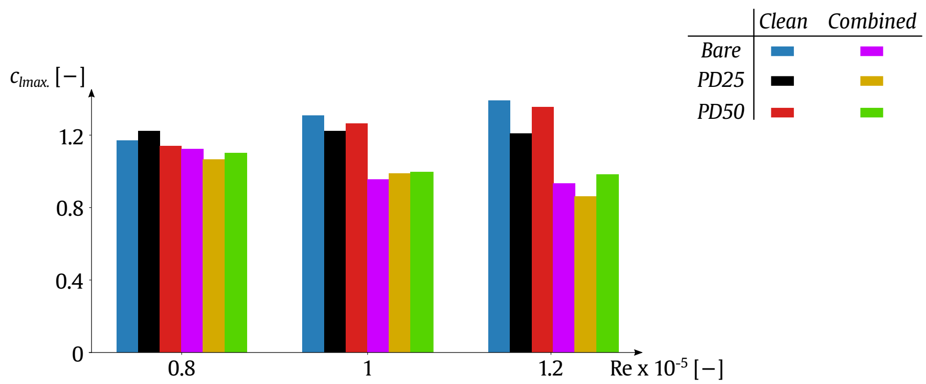

(a) $c_{l_{\max.}}$ parameter.

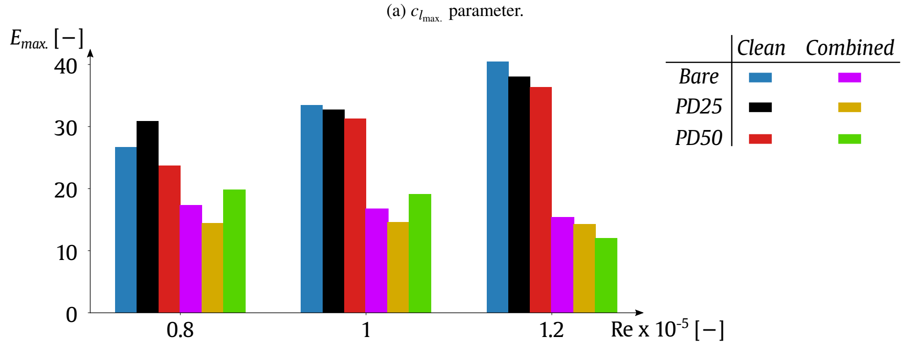

(b) $E_{\max.}$ parameter.

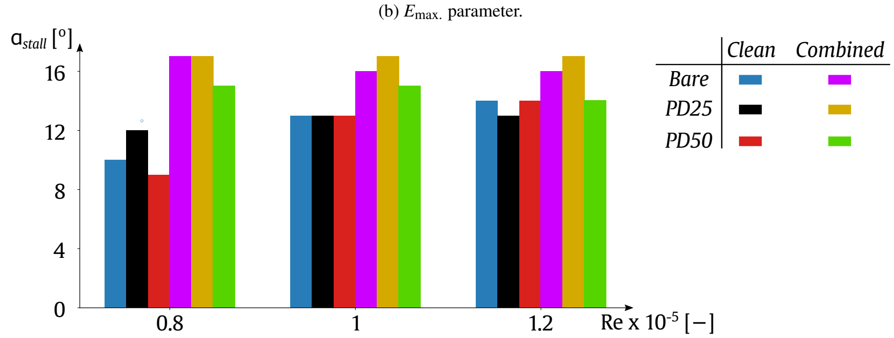

(c) α_{stall} parameter.

FIG. 10: Synthesis of the relevant aerodynamic parameters represented in the characteristic curves.

IV. CONCLUSIONS AND FUTURE WORKS

A NACA0021 airfoil was tested with two unilateral passive-device layouts—*PD25* ($x/c = 0.25$) and *PD50* ($x/c = 0.5$)—under *Clean* and *Combined* (moderate turbulence + leading-edge roughness) inflows over $\text{Re} \in [0.8, 1.2] \times 10^5$. Global metrics ($c_l$, c_d, $E = c_l/c_d$, α_{stall}) were used to quantify trends.

Main aerodynamic findings.

- *Combined* inflow straightens c_l–α (LSB suppression) but lowers lift slope and efficiency: typical E losses span ~ 30–70% relative to *Clean*, while α_{stall} tends to increase (more resilient, partly turbulent layers).

- Unilateral devices introduce a zero-lift offset at $\alpha = 0°$ (sign depends on layout); this offset weakens under *Combined* inflow due to stronger mixing.

- Layout dependence is strong and Re-sensitive: *PD25* can delay stall and recover E at high α (notably at lower Re and under *Combined*); *PD50* yields only narrow, mid-α benefits (most visible around $\text{Re} = 1.0 \times 10^5$ in *Combined*) and is otherwise neutral or detrimental.

- With increasing Re, boundary-layer thickness shrinks; a fixed device height becomes more intrusive ($h/\delta \uparrow$), narrowing the operating window where passive control is beneficial.

Implications.

- Aerodynamic data from *Clean* tunnels overpredict performance in realistic environments; design and validation at low Re should include coexisting turbulence and surface roughness.

- For small-wind and low-Re devices, passive control is effective only in limited α–Re windows; if used, leading-edge layouts (e.g., $x/c \approx 0.25$) should be tuned to the target operating range.

- Mid-chord protrusions are rarely advantageous once the layer is fully turbulent or already separated.

Limitations and future work.

- Add local diagnostics (c_p distributions and oil-flow visualizations) to resolve transition, separation and reattachment under *Combined* inflow, and to map hysteresis with finer α resolution. This research is currently being held by the authors, and future contributions are expected once the c_p post-processing techniques are refined for the *Combined* paradigms, as well as the oil-flow visualization protocols adjusted.

- Systematically vary device geometry (height h, spacing s, multi-row layouts) and quantify robustness versus turbulence spectra and calibrated roughness metrics.

- Extend the Re envelope and translate the airfoil-level trends to rotor performance (power curves, loads, and AEP), including shear/veer and unsteady inflow.

- Explore hybrid strategies: passive leading-edge tripping for stall management combined with operational control (e.g., pitch) for load mitigation and energy-yield recovery.

DATA AVAILABILITY STATEMENT

The data that support the findings of this study are available from the corresponding author upon reasonable request.

[1] Global Wind Energy Council. Global wind report 2025. https://www.gwec.net/events/2025-global-wind-report-launch/, 2025. Accessed April 2025.

[2] International Renewable Energy Agency. Renewable capacity statistics 2025. https://www.irena.org/Publications/2025/Jul/Renewable-energy-statistics-2025, 2025. Accessed May 2025.

[3] Turaj Ashuri, Joaquim RRA Martins, Michiel B Zaaijer, Gijs AM van Kuik, and Gerard JW van Bussel. Aeroservoelastic design definition of a 20 mw common research wind turbine model. *Wind energy*, 19(11):2071–2087, 2016.

[4] B. Amirzadeh, A. Louhghalam, M. Raessi, and M. Tootkaboni. A computational framework for the analysis of rain-induced erosion in wind turbine blades, part I: Stochastic rain texture model and drop impact simulations. *Journal of Wind Engineering and Industrial Aerodynamics*, 163(September 2016):33–43, 2017.

[5] A. Bianchini, G. Bangga, I. Baring-Gould, A. Croce, J. I. Cruz, R. Damiani, G. Erfort, C. Simao Ferreira, D. Infield, C. N. Nayeri, G. Pechlivanoglou, M. Runacres, G. Schepers, B. Summerville, D. Wood, and A. Orrell. Current status and grand challenges for small wind turbine technology. *Wind Energy Science Discussions*, 2022:1–54, 2022.

[6] José Luis Torres-Madroñero, Joham Alvarez-Montoya, Daniel Restrepo-Montoya, Jorge Mario Tamayo-Avendaño, César Nieto-Londoño, and Julián Sierra-Pérez. Technological and operational aspects that limit small wind turbines performance. *Energies*, 13(22):1–39, 2020.

[7] S. Cho. *Control of a flow around a low Reynolds number airfoil using longitudinal strips*. PhD thesis, Seoul National University, Seoul, South Corea, 2019.

[8] Ander Zarketa-astigarraga, Markel Penalba, Alain Martin-mayor, and Manex Martinez-agirre. Experimental assessment of scale-effects on the aerodynamic characterization of a transitionally-operating airfoil working under clean flow conditions. *Measurement*, 188(December 2021):110414, 2022.

[9] Q. Ning, W. Yuan, and T. Wang. Spectral characteristics of roughness-induced transition in low-re airfoils. *Exp. Therm. Fluid Sci.*, 133:110558, 2022.

[10] P. Shah and S. Yarusevych. Mechanisms of boundary-layer transition over rough airfoils at low reynolds numbers. *J. Fluid Mech.*, 956:A31, 2023.

[11] N. Karthikeyan, S. Sudhakar, and P. Suriyanarayanan. Experimental studies on the effect of leading edge tubercles on laminar separation bubble. In *52nd Aerospace Sciences Meeting*, number January, pages 1–16, National Harbor, MA, U.S.A, 2014. American Institute for Aeronautics and Astronautics (AIAA).

[12] G. Ananda, P. Sukumar, and M. Selig. Measured Aerodynamic Characteristics of Wings at Low Reynolds Numbers. *Aerospace Science and Technology*, 42:392–406, 2015. ISSN 12709638.

[13] Longhuan Du, Arganthaël Berson, and Robert G Dominy. Aerofoil behaviour at high angles of attack and at Reynolds numbers appropriate for small wind turbines. *Proceedings of the Institution of Mechanical Engineers, Part C: Journal of Mechanical Engineering Science*, 229(11):2007–2022, 2015.

[14] Xuanshi Meng, Haiyang Hu, Xu Yan, Feng Liu, and Shijun Luo. Lift improvements using duty-cycled plasma actuation at low Reynolds numbers. *Aerospace Science and Technology*, 72:123–133, 2018.

[15] Ander Zarketa-Astigarraga, Alain Martin-Mayor, Manex Martinez-Agirre, and Markel Peñalba-Retes. Assessing the statistical validity of momentum-deficit-based c_D measurements in turbulent configurations. *Measurement*, 181, 2021.

[16] Ander Zarketa-Astigarraga, Markel Penalba, Alain Martin-Mayor, and Manex Martinez-Agirre. Impact of turbulence and blade surface degradation on the annual energy production of small-scale wind turbines. *Wind Energy*, 26:1217 – 1234, 2023. doi:10.1002/we.2866.

[17] A. Zarketa-Astigarraga. *Aerodynamic Characterization of Transitionally-Operating Airfoils under a set of Flow Conditions going from Ideal to Real Configurations*. PhD thesis, Mondragon Goi Eskola Politeknikoa, 2021.

[18]Simon Watkins, Juliette Milbank, Benjamin J. Loxton, and William H. Melbourne. Atmospheric winds and their implications for microair vehicles. 44 (11):2591–2600, . ISSN 0001-1452, 1533-385X.

[19]M. Thompson, S. Watkins, C. White, and J. Holmes. Span-wise wind fluctuations in open terrain as applicable to small flying craft. 115(1173):693–701. ISSN 0001-9240, 2059-6464.

[20]S Watkins, J Burry, A Mohamed, M Marino, S Prudden, A Fisher, N Kloet, T Jakobi, and R Clothier. Ten questions concerning the use of drones in urban environments. 167:106458, . ISSN 03601323.

[21]Anup KC, Jonathan Whale, and Tania Urmee. Urban wind conditions and small wind turbines in the built environment: A review. *Renewable Energy*, 131:268–283, 2019.

[22]Anup Kc, Jonathan Whale, Samuel P Evans, and Philip D Clausen. An investigation of the impact of wind speed and turbulence on small wind turbine operation and fatigue loads. *Renewable Energy*, 146:87–98, 2020.

[23]J. Li, Y. Gao, and L. Zhao. Influence of inflow turbulence generated by passive grids on airfoil performance at transitional reynolds numbers. *Wind Energy Sci.*, 7:1331–1347, 2022.

[24]J. P. Bons. A review of surface roughness effects in gas turbines. 132(2): 021004.

[25]K. A. Flack, M. P. Schultz, and J. M. Barros. Skin friction measurements of systematically-varied roughness: Probing the role of roughness amplitude and skewness. 104(2):317–329. ISSN 1386-6184, 1573-1987.

[26]Ali Zamiri, Sung Jin You, and Jin Taek Chung. Surface roughness effects on film-cooling effectiveness in a fan-shaped cooling hole. 119:107082.

[27]Gustave P. Corten and Herman F. Veldkamp. Aerodynamics: Insects can halve wind-turbine power. *Nature*, 412(6842):41–42, 2001.

[28]Mohammed G. Khalfallah and Aboelyazied M. Koliub. Effect of dust on the performance of wind turbines. *Desalination*, 209:209–220, 2007.

[29]Agrim Sareen, Robert W. Deters, Steven P. Henry, and Michael S. Selig. Drag Reduction Using Riblet Film Applied to Airfoils for Wind Turbines. *Journal of Solar Energy Engineering*, 136(2):021007, 2013.

[30]Woobeom Han, Jonghwa Kim, and Bumsuk Kim. Effects of contamination and erosion at the leading edge of blade tip airfoils on the annual energy production of wind turbines. *Renewable Energy*, 115:817–823, 2018.

[31]Kostas Latoufis, Vasilis Riziotis, Spyros Voutsinas, and Nikos Hatziargyriou. Effects of Leading Edge Erosion on the Power Performance and Acoustic Noise Emissions of Locally Manufactured Small Wind Turbine Blades. *Journal of Physics: Conference Series*, 1222(1):1–12, 2019.

[32]Rodolfo Curci, Puraca Bruno, and Souza Carmo. Analysis of wind turbine blade aerodynamic optimization strategies considering surface degradation. *Journal of the Brazilian Society of Mechanical Sciences and Engineering*, 43(10):1–22, 2021.

[33]Luis Bartolomé and Julie Teuwen. Prospective challenges in the experimentation of the rain erosion on the leading edge of wind turbine blades. *Wind Energy*, 22(1):140–151, 2019.

[34]Ibrahim Mohamed Elhadi and Medraj Mamoun. Water Droplet Erosion of Wind Turbine Blades: Mechanics, Testing, Modeling and Future Perspectives. *Materials*, 13(157):1 – 33, 2020.

[35]Hamish Law and Vasileios Koutsos. Leading edge erosion of wind turbines: Effect of solid airborne particles and rain on operational wind farms. *Wind Energy*, 23(10):1955–1965, 2020.

[36]L. Mydlarski. Generation of high-reynolds-number grid turbulence. *Annu. Rev. Fluid Mech.*, 46:457–482, 2014.

[37]F. Castellani, A. Vignaroli, and D. Astolfi. Experimental characterisation of turbulence intensity effects on small-scale wind-turbine aerodynamics. *Renew. Energy*, 125:425–435, 2018.

[38]S Farshid Chini, M Mahmoodi, and M Nosratollahi. The Potential of Using Superhydrophobic Surfaces on Airfoils and Hydrofoils: a Numerical Approach. *International Journal of Computational Materials Science and Surface Engineering*, 7(1):44, 2017.

[39]Linyue Gao, Hui Zhang, Yongqian Liu, and Shuang Han. Effects of vortex generators on a blunt trailing-edge airfoil for wind turbines. *Renewable Energy*, 76:303–311, 2015.

[40]Z. Wang, J. Chen, and F. Xu. Passive flow control of transitional airfoils under turbulent inflow conditions. *Aerospace Sci. Technol.*, 151:108308, 2024.

[41]Serhiy Yarusevych and Marios Kotsonis. Effect of Local DBD Plasma Actuation on Transition in a Laminar Separation Bubble. *Flow, Turbulence and Combustion*, 98(1):195–216, 2017.

[42]Lennart S. Hultgren and David E. Ashpis. Demonstration of separation control using dielectric barrier discharge plasma actuators. *AIAA Journal*, 56(11):4614–4620, 2018.

[43]R. Ricci, S. Montelpare, and E. Renzi. Study of Mechanical Disturbances Effects on the Laminar Separation Bubble by Means of Infrared Thermography. *International Journal of Thermal Sciences*, 50(11):2091–2103, 2011.

[44]A. Panta, A. Mohamed, M. Marino, S. Watkins, and A. Fisher. Unconventional control solutions for small fixed wing unmanned aircraft. *Progress in Aerospace Sciences*, 102(May):122–135, 2018.

[45]R. Ricci, S. Montelpare, and E. Silvi. Study of Acoustic Disturbances Effect on Laminar Separation Bubble by IR Thermography. *Experimental Thermal and Fluid Science*, 31(4):349–359, 2007.

[46]R. Ricci and S. Montelpare. Analysis of Boundary Layer Separation Phenomena by Infrared Thermography Use of Acoustic and/or Mechanical Devices to Avoid or Reduce the Laminar Separation Bubble Effects. *Quantitative InfraRed Thermography Journal*, 6(1):101–125, 2009.

[47]Brian Dean and Bharat Bhushan. Shark-skin surfaces for fluid-drag reduction in turbulent flow: A review. *Philosophical Transactions of the Royal Society A: Mathematical, Physical and Engineering Sciences*, 368(1929): 4775–4806, 2010.

[48]Mariana Kok and Trevor M. Young. The evaluation of hierarchical structured superhydrophobic coatings for the alleviation of insect residue to aircraft laminar flow surfaces. *Applied Surface Science*, 314:1053–1062, 2014.

[49]S. Shahinfar, S. Sattarzadeh, J. Fransson, and A. Talamelli. Revival of Classical Vortex Generators now for Transition Delay. *Physical Review Letters*, 109:1–5, 2012.

[50]Hanns Mueller-Vahl, Georgios Pechlivanoglou, C. N. Nayeri, and C. O. Paschereit. Vortex generators for wind turbine blades: a combined wind tunnel and wind turbine parametric study. In *Proceedings of ASME Turbo Expo 2012*, pages 1–16. ASME, 2012.

[51]M. O. L Hansen, C. M Velte, S. ØYe, R. Hansen, N. N. Sørensen, J. Madsen, and R. Mikkelsen. Aerodynamically shaped vortex generators. *Wind Energy*, 18(11):1875–1891, 2015.

[52]R. Sun, X. Liu, and H. Zhang. Experimental study of discrete-roughness-element control on a low-re airfoil. *Exp. Fluids*, 64:115, 2023.

[53]Ivan Torrano. *Low speed wind tunnel design, setup, validation and testing of airfoils in turbulent in ow conditions*. PhD thesis, Mondragon Goi Eskola Politeknikoa, 2016.

[54]Ander Zarketa-Astigarraga, Alain Martin-Mayor, and Manex Martinez-Agirre. Experimental uncertainty decompositions of aerodynamic coefficients affected by operative condition variations. *Measurement*, 165(C): 1–14, 2020.

[55]Mark Drela and Michael B. Giles. Viscous-inviscid analysis of transonic and low Reynolds number airfoils. *AIAA Journal*, 25(10):1347–1355, 1987.

[56]José Meseguer-Ruiz and Ángel Sanz-Andrés. Procedimientos para determinar numéricamente la resistencia. In *Aerodinámica Básica*, chapter 9.2, pages 262–264. Garceta Grupo Editorial, 2 edition, 2012.

[57]Labview software main page. URL https://www.ni.com/en-us/shop/labview.html.

[58]Anup KC, Jonathan Whale, and Joachim Peinke. An investigation of the impact of turbulence intermittency on the rotor loads of a small wind turbine. *Renewable Energy*, 169:582–597, 2021.

[59]Ander Zarketa-Astigarraga, Alain Martin-Mayor, and Manex Martinez-Agirre. Theoretical concepts for describing a replication-levels-based uncertainty analysis approach. In Sergey Yurish, editor, *Advances in Measurements and Instrumentation: Reviews, Book Series, Vol. 2*. IFSA Publishing, 1 edition, 2020.

[60]J. S. Kline and F. A. McClintock. Uncertainties in single-sample experiments. *Mechanical Engineering*, pages 3–8, 1953.

[61]I. M. M. A. Shabaka, R. D. Mehta, and P. Bradshaw. Longitudinal vortices imbedded in turbulent boundary layers. part 1. single vortex. *Journal of Fluid Mechanics*, 155:37–57, 1985.

[62]Timothy Jukes, Kwing-So Choi, Graham Johnson, and Simon Scott. *Turbulent Drag Reduction by Surface Plasma Through Spanwise Flow Oscillation*. doi:10.2514/6.2006-3693.